Title
Photodissociation of iso-propoxy (i-C 3 H 7 O) radical at 248 nm

Journal
Physical Chemistry Chemical Physics, 22(31)

ISSN
1463-9076

Authors
Sullivan, Erin N
Saric, Steven
Neumark, Daniel M

Publication Date
2020-08-21

DOI
10.1039/d0cp02493g

Peer reviewed

Photodissociation of *iso*-Propoxy (*i*-C_3H_7O) Radical at 248 nm

Erin N. Sullivan, Steven Saric and Daniel M. Neumark[1]

Department of Chemistry, University of California, Berkeley, California 94720, USA and Chemical Sciences Division, Lawrence Berkeley National Laboratory, Berkeley, California 94720, USA

Abstract:

Photodissociation of the *i*-C_3H_7O radical is investigated using fast beam photofragment translational spectroscopy. Neutral *i*-C_3H_7O radicals are produced through the photodetachment of a fast beam of *i*-$C_3H_7O^-$ anions and are subsequently dissociated at 248 nm (5.0 eV). The dominant product channels are CH_3 + CH_3CHO and OH + C_3H_6 with some contribution from H + C_3H_6O. The CH_3 and H loss channels are attributed to dissociation on the ground electronic state of *i*-C_3H_7O, but in a nonstatistical manner because calculated RRKM dissociation rates exceed the rate of energy randomization. Translational energy and angular distributions for OH loss are consistent with ground state dissociation, but the branching ratio for this channel is considerably higher than predicted from RRKM rate calculations. Additionally, *i*-C_3H_7O undergoes three-body fragmentation to CH_3 + CH_3 + HCO and CH_3 + CH_4 + CO. These three-body channels are attributed to dissociation of *i*-C_3H_7O to CH_3 + CH_3CHO, followed by secondary dissociation of CH_3CHO on its ground electronic state.

[1] Corresponding author. Email: dneumark@berkeley.edu

1. Introduction:

Alkoxy radicals (RO) are crucial players in atmospheric chemistry processes in which the oxidation of hydrocarbons propagates numerous reaction chains through interactions with O_2 and the NO_x cycle.[1,2] Larger RO species have been implicated in autoignition chemistries,[3,4] and the reactions of alkenes with OH radicals, through which RO radicals can be generated, are key steps in combustion schemes.[5] As such, understanding the fundamental properties and behaviors of these radicals is of general interest, and there is a wealth of information regarding the smallest RO radicals: CH_3O, C_2H_5O, C_3H_7O, and *t*-C_4H_9O.[6,7] In our laboratory, we have previously investigated photodissociation of CH_3O and C_2H_5O;[8,9] here, we present the results of *i*-C_3H_7O ($(CH_3)_2CHO\cdot$) dissociation at 248 nm using fast radical beam photofragment translational spectroscopy and compare the results to the smaller alkoxy radicals.

i-C_3H_7O is of general interest as a larger member of the alkoxy family and can occur as multiple isomers as shown in Figure 1. *i*-C_3H_7O, as opposed to *n*-C_3H_7O, was chosen here due to the ease of generating its anionic precursor from isopropanol. Additionally, there is a larger body of work in the literature examining *i*-C_3H_7O, although *n*-C_3H_7O has not been entirely neglected. The simplest alkoxy radical CH_3O belongs to the C_{3v} point group with distinct $\tilde{X}(^2E)$ and $\tilde{A}(^2A_1)$ states separated in energy by several eV.[6,8] However, in the *i*-C_3H_7O radical, C_{3v} symmetry is broken by the additional methyl groups, and the ground state is split into two nearly degenerate electronic states, which for *i*-C_3H_7O are the $\tilde{X}(^2A')$ and $\tilde{A}(^2A'')$ states.

The laser fluorescence spectrum of *i*-C_3H_7O was first measured by Foster et al.[10,11] and revisited by Liu et al.[12,13] who characterized the $\tilde{B} \leftarrow \tilde{X}$ transition and determined the term value of the $\tilde{B}(^2A')$ state to be 27164.4 cm^{-1}. The authors found parallel-type line intensities associated with this transition and assigned the ground electronic state of *i*-C_3H_7O to A' symmetry, in contrast to the A'' ground state of the ethoxy radical (C_2H_5O).[12] In addition to characterizing the higher-lying $\tilde{B}$ state, laser induced fluorescence determined the energetic splitting of the $\tilde{A}$ and $\tilde{X}$ states to be 60.4 cm^{-1}. Further exploration of the $\tilde{B} \leftarrow \tilde{X}$ and $\tilde{B} \leftarrow \tilde{A}$ transitions examined the effect of pseudo-Jahn-Teller distortion in vibronic coupling between the $\tilde{X}\ ^2A'$ and $\tilde{A}\ ^2A''$ states.[12] The anion photoelectron spectrum of *i*-$C_3H_7O^-$ has been measured previously,[6,14] and the electron affinity of the *i*-C_3H_7O radical was determined to be 1.847 ± 0.004 eV. As in the fluorescence

spectrum, the photoelectron spectrum is complicated by vibronic coupling between the $\tilde{X}$ and $\tilde{A}$ states. Dillon et al.[15] analyzed the photoelectron spectrum in detail and confirmed 68 cm^{-1} as the $\tilde{A}$ and $\tilde{X}$ splitting.

Several studies have examined the experimental association of OH + C_3H_6 (propene) that can, in principle, yield *i*-C_3H_7O.[16-19] Theoretical work[20] indicates that OH addition to the central carbon of propene yields $CH_3CHOHC{\cdot}H_2$, which can then isomerize to *i*-C_3H_7O ($(CH_3)_2CHO{\cdot}$). These studies implicate OH + C_3H_6 as a potential product channel for *i*-C_3H_7O dissociation.

The photodissociation of *i*-C_3H_7O has yet to be explored, but that of its close counterpart, C_2H_5O, has been investigated at 5.17 eV and 5.96 eV.[9] The predominant photofragments observed were OH + C_2H_4 and CH_3 + CH_2O, and dissociation experiments of the isotopologue C_2D_5O identified D + C_2D_4O as a valid product channel.[9] No three-body dissociation was observed.

In this work, photofragment translational spectroscopy was used to examine the photodissociation of *i*-C_3H_7O at 248 nm (5.0 eV). Equations 1 through 11 present the possible product channels at this energy.[5,6,21]

i-C_3H_7O	→ CH_3 + CH_3CHO (acetaldehyde)	D_0 = 0.29 eV	(1)
	→ H + $(CH_3)_2CO$ (acetone)	D_0 = 0.50 eV	(2)
	→ CH_3 + C_2H_3OH (vinyl alcohol)	D_0 = 0.72 eV	(3)
	→ H + C_3H_5OH (2-propenol)	D_0 = 0.92 eV	(4)
	→ OH + C_3H_6	D_0 = 1.08 eV	(5)
	→ H + c-C_3H_5OH (cyclopropanol)	D_0 = 1.64 eV	(6)
	→ H + c-$C_2H_3O(CH_3)$ (epoxypropane)	D_0 = 1.76 eV	(7)
	→ O (^{3}P) + C_3H_7	D_0 = 3.97 eV	(8)
	→ CH_3 + CH_4 + CO	D_0 = 0.09 eV	(9)
	→ CH_3 + CH_3 + HCO	D_0 = 3.95 eV	(10)
	→ H + CH_3 + C_2H_3O	D_0 = 4.16 eV	(11)

Figure 1 shows the lower energy two-body product channels and the pathways through isomers $CH_3C{\cdot}(OH)CH_3$ (hydroxy carbenyl) and/or $CH_3CHOHC{\cdot}H_2$ (hydroxy propenyl). The predominant two-body channel observed is consistent with channel 1 (CH_3 + CH_3CHO) with some contribution from channel 5 (OH + C_3H_6) and a H loss channel, either channel 2 (H +

$(CH_3)_2CO$) or 4 (H + C_3H_5OH). Additionally, a small amount of three-body dissociation is observed through channels 9 (CH_3 + CH_4 + CO) and 10 (CH_3 + CH_3 + HCO) through secondary dissociation of acetaldehyde.

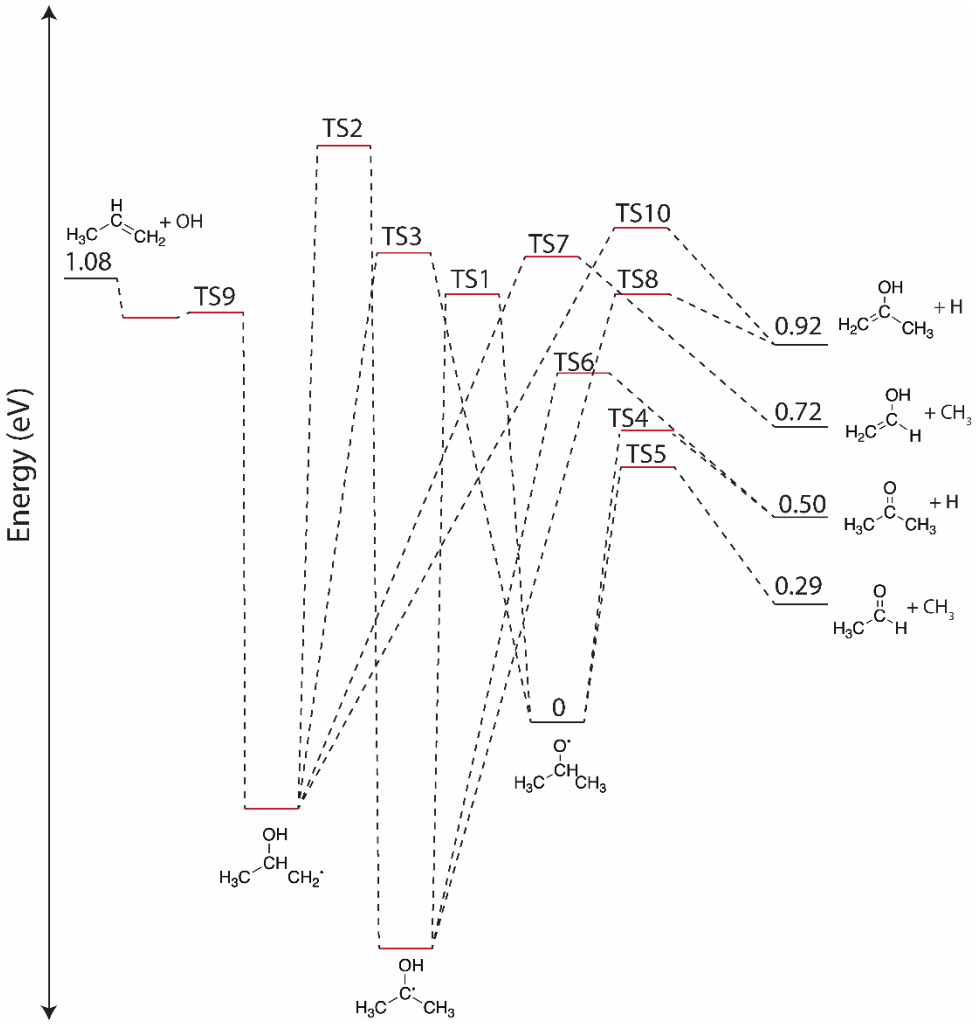

Figure 1: Potential energy surface for the lowest energy two-body dissociation pathways of *i*-C_3H_7O. The product energies are determined from experimental heats of formation.[21] The energies of structures and transition states marked by a red line were acquired from Reference 5.

2. Experimental Methods:

The fast radical beam instrument has been presented in detail previously.[22-24] In brief, 40 psig of Ar/He was bubbled through isopropanol (99.5% Millipore) and expanded into vacuum through a pulsed Amsterdam Piezovalve[25,26] operating at 100 Hz. *i*-$C_3H_7O^-$ anions were generated when the gas was expanded through a DC discharge grid. The anions were accelerated to 6-8 keV, mass selected using a Bakker time-of-flight mass spectrometer,[27,28] compressed, and steered. A light pulse at 532 nm (2.33 eV) from a Nd:YAG (Litron 742-100) laser or 655 nm from a

Nd:YAG-pumped dye laser (Radiant Dyes Narrowscan) intersected the anions and detached an electron to generate a fast beam of *i*-C_3H_7O radicals. Deuterated experiments were performed in a similar manner using deuterated isopropanol (99.5% Sigma Aldrich) as a precursor.

A photoelectron spectrometer mounted perpendicular to the ion beam direction measured the kinetic energy of the detached electrons.[24] Following detachment, electrons were velocity-map-imaged on to a microchannel plate detector coupled to a phosphor screen and CCD camera (Beam Imaging Solutions BOS-75).[24] The acquired images were analyzed using the Inverse Abel transformation (BASEX).[29] Multiple detachment wavelengths (λ_{detach}) were used to properly minimize the internal energy of the resultant *i*-C_3H_7O radicals and characterize its effect in the dissociation results.

Following photodetachment, *i*-C_3H_7O radicals were intersected by 248 nm (5.0 eV) light from a GAM EX50 excimer laser. Two- and three-body fragments were collected in coincidence using a time-and-position sensitive Roentdek Hex80 delay-line detector.[30,31] A 2.9 mm radius beam block near the center of the detector face prevented undissociated radicals from impinging upon the detector. The arrival times and positions of fragments in coincidence were used to generate photofragment mass, translational energy, and angular distributions. The translational energy distributions presented here have been corrected using a detector acceptance function (DAF) to account for the beam block and finite size of the detector.[24]

The translational energy and angular distributions are given by

$$P(E_T, \theta) = P(E_T) \cdot [1 + \beta(E_T) P_2(\cos\theta)] \quad (12)$$

in which $\beta(E_T)$ is the energy-dependent anisotropy parameter and $P_2(\cos\theta)$ is the second Legendre polynomial.[32] For experiments performed using linearly polarized light, θ is the angle between the electric field vector and dissociation recoil axis such that β_{lin} varies from -1 to 2 for pure perpendicular and parallel transitions, respectively. However, in our experiments, in which the output of the excimer laser is unpolarized, θ is referenced to the laser propagation direction as opposed to the electric field vector. As such, for two-body dissociation processes, θ is defined as the angle between the laser propagation direction and dissociation recoil axis. One can show that $\beta_{obs} = -\beta_{lin}/2$ and thus ranges from ½ to -1 for perpendicular and parallel processes,

respectively.[24] For three-body processes, θ is defined as the angle between the laser propagation direction and the normal to the plane of dissociation.

Owing to the high product mass ratio (58:1) of channels that involve H loss (channel 2 or 4), these channels cannot be detected in coincidence because the H atom generally scatters beyond the detector and the heavy fragment hits the beam block. However, for events with sufficient translational energy release, the heavy fragment can travel enough distance in the plane parallel to the detector to clear the beam block and be detected. By collecting the time-of-flight distribution of all fragments that hit the detector, we can learn about H loss channels through simulations. This measurement is more effective for the deuterated isotopologue and is discussed in Section 3.d.

3. Results:

a. Anion photoelectron spectrum

The anion photoelectron spectrum of *i*-$C_3H_7O^-$ is presented in Figure 2. The black trace is the experimental distribution using a detachment wavelength of 532 nm.

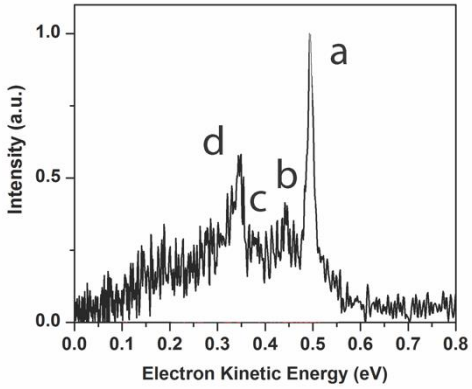

Figure 2: Photoelectron spectrum of *i*-$C_3H_7O^-$ at 532 nm as a function of electron kinetic energy (eKE).

The largest feature, peak a, corresponds to the vibrational origin (the 0-0 transition) yielding an electron affinity of 1.836 ± 0.005 eV that matches previously reported values.[6,13] Hence we can identify the radical produced by photodetachment to be *i*-C_3H_7O. The photoelectron spectrum is consistent with that reported by Ramond et al.[6] who observed an intense, well-defined feature corresponding to the origin and numerous less-defined peaks at lower kinetic energies. The use

of isopropanol as a starting material preferentially leads to *i*-C_3H_7O formation with high barriers to formation of other isomers. Furthermore, the electron affinities of the hydroxy alkyl radicals have been predicted to be < 1 eV.[33] Therefore, $(CH_3)_2C{\cdot}OH$ and $CH_3CHOHC{\cdot}H_2$ would have distinct photoelectron spectra with much higher electron kinetic energies. As such, *i*-C_3H_7O is the primary species generated here. The features labelled b and c in Fig. 2 were previously assigned to one quantum of excitation in the CCC bend and the CCCO symmetric bending mode, respectively.

The photoelectron spectrum can also be used to characterize the internal energy of the generated radical. In Fig. 2, λ_{detach} = 532 nm (2.33 eV) which is ~ 0.5 eV above the electron affinity of *i*-C_3H_7O. Despite this, most of the radicals are generated in their ground vibrational state, as is evident by the dominant vibrational origin. The majority of the dissociation data presented in the following sections is for experiments performed with λ_{detach} = 655 nm (1.89 eV), which is just above the electron affinity of *i*-C_3H_7O. We thus approximate the internal energy of the *i*-C_3H_7O radicals $E_{\mathrm{INT}}^{\mathrm{R}}$ to 0 eV in subsequent analysis.

b. Mass distributions

a) b)

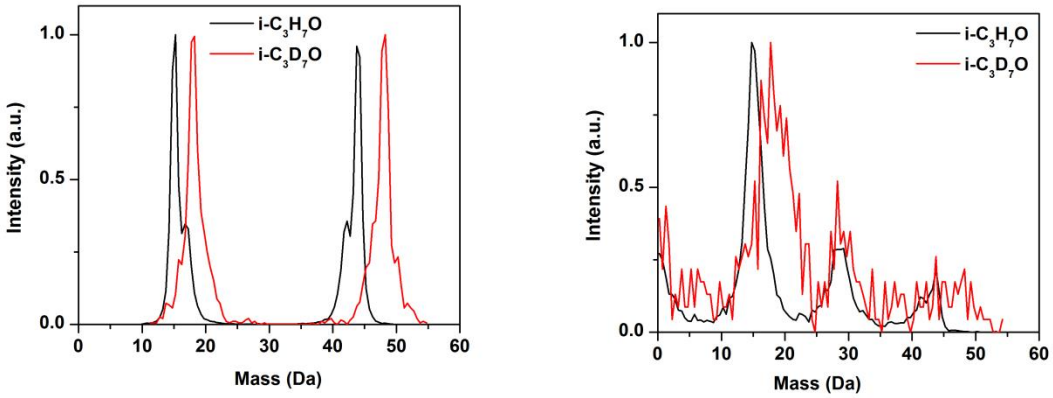

Figure 3: Two-body (a) and three-body (b) mass distributions of *i*-C_3H_7O dissociation via 248 nm. The black traces present the results of *i*-C_3H_7O dissociation, and the red traces present the results of *i*-C_3D_7O dissociation.

Figure 3 presents the mass distributions for dissociation of *i*-C_3H_7O (black traces) and *i*-C_3D_7O (red traces) at 248 nm. Fig. 3a shows the two-body mass distribution in which the black trace exhibits narrow features around 15 Da and 44 Da with distinctive shoulders on each peak. The

well-defined features are consistent with true two-body dissociation. The main peaks at 15 Da and 44 Da correspond to CH_3 and C_2H_4O. As such, these features are due to either channel 1 ($CH_3 + CH_3CHO$) or 3 ($CH_3 + C_2H_3OH$). The shoulders on the main features extend to ~17 Da and 42 Da and thus suggest the formation of $O + C_3H_7$ (channel 8), $OH + C_3H_6$ (channel 5) or both. In dissociating *i*-C_3D_7O, which is shown in red, the lower mass peak shifts to 18 Da, and the higher mass peak shifts to 48 Da. These shifts are consistent with the formation of channel 1 and/or 3 in which CH_3 (15 Da) shifts to CD_3 (18 Da), and the C_2D_4O co-fragment appears at 48 Da. Additionally, the shoulder in the red trace is less distinct, suggesting that the mass of the secondary channel is identical to channel 1 or 3 upon deuteration (18 Da and 48 Da), thereby confirming the assignment of channel 5 ($OH + C_3H_6$). To further analyze these results, the mass distributions were simulated using the translational energy distributions of channels 1 and 5 and were found to be consistent with the experimental results. These are presented in Figure S1 in the supplementary material and confirm the absence of channel 8.

Figure 3b presents the three-body mass distribution for the dissociation of *i*-C_3H_7O (black) and *i*-C_3D_7O (red) at 248 nm. The most noticeable feature in the black trace is a peak around 15-16 Da that is ~3-4 times more intense than any other feature. In examining the possible three-body product channels, 9-11, one can see that CH_3 is a product for all three channels. The second fragment for channels 9 ($CH_3 + CH_4 + CO$) or 10 ($CH_3 + CH_3 + HCO$) is either CH_4 or CH_3, respectively. Thus, the presence of a second fragment attributed to either CH_3 or CH_4 explains the intensity of this main feature. Additionally, there is a broad feature spanning ~26-31 Da which could be from CO (28 Da), HCO (29 Da) or both.

The photodissociation of *i*-C_3D_7O is again useful in assessing the contributions of channels 9 and 10. The red distribution is significantly noisier than the black one owing to substantially fewer coincidence events collected for the deuterated radical. The peak at 15 Da (CH_3) shifts to 18 Da as expected, but it also noticeably widens, which would occur if we were observing both CD_3 (18 Da) and CD_4 (20 Da). Furthermore, the broad feature spanning 28-29 Da is slightly extended on the high-mass edge in the deuterated distribution, which might occur if both CO (28 Da) and DCO (30 Da) were present. As such, the deuterated distribution suggests that both channel 9 and 10 are formed.

Finally, there is a feature at 1 Da (corresponding to the H atom) and 43 Da (C_2H_3O) which could be from channel 11 (H + CH_3 + C_2H_3O). However, in examining the deuterated distribution, it is not obvious that a shift from 1 Da (H) to 2 Da (D) is present. Additionally, coincident dissociation events resulting in H atom loss are often suspect in our experiment as they can arise from false coincidence events associated with the challenges of detecting H atoms in our experimental setup. Indeed, false coincidence simulations, presented and described in the supplementary material (Figure S2) lead us to conclude that most of this signal at 1 Da results from artifacts of the detection scheme rather than true channel 11 formation. As such, this channel will not be discussed further.

c. Translational energy distributions

The translational energy imparted to photofragments is given by

$$E_T = h\nu - D_0 + E_{INT}^R - E_{INT}^P \qquad (13)$$

in which E_T is the translational energy of the photofragments, $h\nu$ is the photon energy (5.0 eV), D_0 is the product channel dissociation energy, E_{INT}^R is the internal energy of the initial *i*-C_3H_7O radical, and E_{INT}^P is the internal energy of the photofragments. As was discussed in Section 3.a, we approximate E_{INT}^R to be 0.

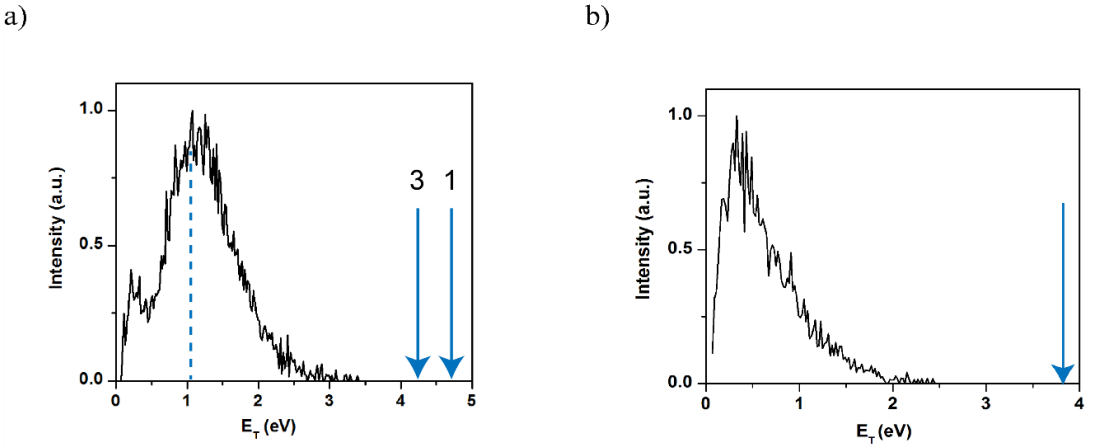

Figure 4: The translational energy distribution of *i*-C_3H_7O dissociation to channel 1 or 3 (CH_3 + CH_3CHO or C_2H_3OH) is shown in panel a in which λ_{detach} = 655 nm. Panel b shows the dissociation of *i*-C_3H_7O to channel 5 (OH + C_3H_6). The maximum available energies ($E_{T,MAX}$) for channels 1, 3 and 5 are marked by blue arrows in the respective panels. Channel 1 products formed with less than 1.05 eV of translational energy (blue dashed line, panel a) can fall apart further.

Figure 4 shows the translational energy distributions of *i*-C_3H_7O dissociation to channel 1 or 3 (CH_3 + CH_3CHO or C_2H_3OH) in panel a and dissociation to channel 5 (OH + C_3H_6) in panel b. In panel a, the distribution is generally broad and peaks around ~1.0-1.5 eV, far below the maximum available energy, $E_{T,MAX}$, which is 4.71 eV and 4.28 eV, for channels 1 and 3, respectively. The anisotropy parameter associated with the main body of the high energy peak is $\beta_{obs} = 0.11 \pm 0.05$ (1-σ error bar) which corresponds to $\beta_{lin} = -0.22 \pm 0.10$. This value is consistent with a perpendicular electronic transition, although the anisotropy is quite weak.

Also noticeable in Figure 4a is a small, broad peak from 0-0.5 eV. Experiments performed with the dissociation laser off indicate that this feature actually stems from dissociation from the detachment laser alone, i.e. a second photon from that laser is absorbed by the radical created by photodetachment. Figure S3a in the supplementary material compares the translational energy distributions for channel 1/3 formation at detachment wavelengths of 532 nm (2.33 eV) and 655 nm (1.89 eV). In the distribution for 532 nm, there is an intense feature peaking around 0.25 eV that mostly disappears in the 655 nm distribution. Moreover, in acquiring dissociation data from the 532 nm detachment laser only, we clearly see in Figure S3b that this low translational energy peak is due to the detachment laser. Therefore, we do not consider the low energy peak in our analysis. Finally, if the C_2H_4O isomer corresponds to CH_3CHO (acetaldehyde) of channel 1, then any events in which the translational energy release is less than 1.05 eV can yield secondary dissociation of the acetaldehyde to channels 9 or 10. As such, this lower energy feature would not likely appear in the distribution, consistent with assigning it to photodissociation from the detachment laser pulse.

Fig. 4b presents the translational energy distribution for formation of channel 5 (OH + C_3H_6). The distribution peaks around 0.5 eV, and tails off by 2.0 eV, well below the blue arrow denoting $E_{T,MAX}$ at 3.92 eV. Channel 5 is also affected by dissociation from the detachment laser only, but as previously indicated, this occurs minimally at λ_{detach} = 655 nm and therefore is not considered a major component of Fig. 4b. The associated angular distribution has $\beta_{obs} = -0.06 \pm 0.13$ and is thus isotropic within our error bars.

a)

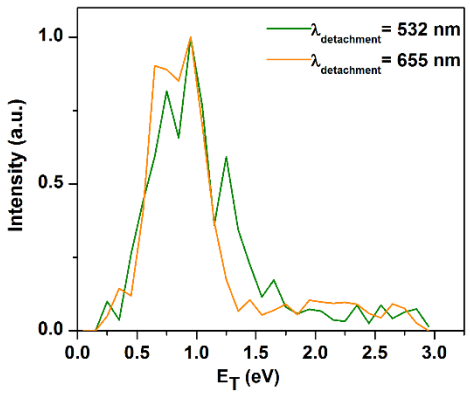

b)

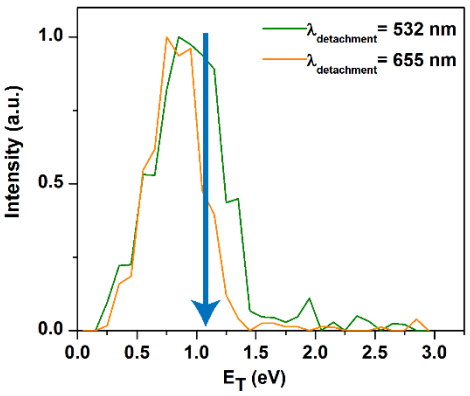

Figure 5: The translational energy distributions of *i*-C_3H_7O dissociation to channel 9 (CH_3 + CH_4 + CO) in panel a and channel 10 (CH_3 + CH_3 +HCO) in panel b. The results for experiments performed at λ_{detach} = 532 nm and λ_{detach} = 655 nm are presented in green and orange, respectively, for comparison. The blue arrow marks the maximum available energy, $E_{T,MAX}$, for channel 10. $E_{T,MAX}$ for channel 9 is off the scale of the x-axis.

Figure 5 presents the translational energy distribution for three-body dissociation channels 9 (CH_3 + CH_4 + CO) and 10 (CH_3 + CH_3 + HCO). Distributions are presented for experiments in which λ_{detach} = 655 nm (orange trace) and λ_{detach} = 532 nm (green trace) to demonstrate the effect of the detachment wavelength. In Fig. 5b, the orange trace tails off at a slightly lower energy than the green trace, but this is not quite as distinct in Fig. 5a. Both sets of distributions look markedly similar, peaking around 0.75 eV and mostly tailing off by $E_{T,MAX}$. However, in Fig. 5a there is a high energy tail that extends out to about 3 eV for both detachment wavelengths

and is mostly absent in Fig. 5b. Due to the low raw experimental counts of these two channels, the anisotropy parameters are not included here.

In Fig. 5b, the distributions for channel 10 formation extend slightly beyond $E_{T,MAX}$, but this can be explained by possible contamination by events of channel 9. Because channels 9 and 10 have products very close in mass, it is likely that some CH_3 is identified as CH_4 and vice versa. This scenario has been observed in our experiment previously for three-body channels with fragments close in mass.[34,35] As such, the similarity of distributions presented in Fig. 5a and 5b is not entirely surprising. Nonetheless, the high energy tail in Fig. 5a suggests that channel 9 is definitely present and is somewhat distinguishable from channel 10.

Three-body dissociation events in our experiment can be further analyzed using Dalitz plots[36] in which the fraction of translational energy imparted to each fragment in a three-body event is characterized. Figure 6 presents the Dalitz plots for channel 9 (panel a) and channel 10 (panel b) formation. ε_i represents the fraction of translation energy imparted to each fragment where $0 \leq \varepsilon_i \leq 1$. Because channel 10 has two fragments of the same mass, events are only plotted for one of the fragments in Fig. 6b. There is a broad swatch of intensity at the right edge of the ellipse (highlighted by the pink dashed line) where the maximum fraction of translational energy is imparted to the CH_3 fragment and the remainder is relatively uniformly distributed across the other two fragments. The plot in Fig. 6a looks similar to that of Fig. 6b except that because each fragment has a different mass, the entire ellipse is plotted and is semi-symmetric about the blue line. There is a broad area of intensity on each edge of the ellipse, again symmetric about the blue line. However, as discussed earlier, the possible misassignment of CH_3 and CH_4 fragments may indicate that one side of the ellipse exhibits intensity that is really due to the alternate fragment. In both plots, the intensity at the right edge of the ellipse implies a high fraction of translational energy imparted to the CH_3 fragment (red arrow).

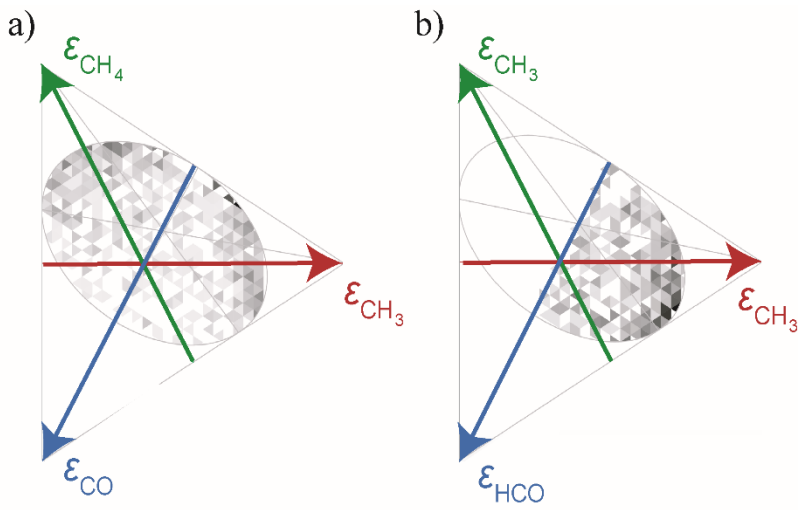

Figure 6: Dalitz plots for three-body dissociation of *i*-C_3H_7O into channel 9 (CH_3 + CH_4 + CO) in panel a and channel 10 (CH_3 + CH_3 + HCO) in panel b.

Three-body dissociation events can be concerted or sequential.[37] Concerted mechanisms are further categorized into synchronous, in which three-fragments form spontaneously, or asynchronous concerted, in which three-fragments are formed on a timescale less than a rotational period of the molecule. Sequential events are those in which two distinct dissociation events occur on a timescale slower than the rotational period of the molecule to ultimately yield three fragments. Sequential events are generally identified by the partitioning of a relatively constant fraction of the translational energy to one fragment. As discussed above, one CH_3 fragment (red arrow) receives a generally high fraction of the total translational energy, which is indicative of it leaving first, followed by dissociation of the remaining CH_3CHO fragment, in support of an asynchronous concerted or sequential mechanism. However, sequential events are usually identified by well-defined fractions of translational energy in one-fragment, such as in the fragmentation of I_2Br^- or CO_3^{2+},[38,39] and the appearance of the Dalitz plots in Fig. 6 are generally broad. As such, channels 9 and 10 may most appropriately be categorized as asynchronous concerted. Figure S4 in the supplementary material presents Newton diagrams that map the center-of-mass momentum vectors for each fragment and bolster our argument that a sequential mechanism is not occurring.

d. Noncoincidence time-of-flight simulations

It has been shown previously that the photodissociation of CH_3O and C_2H_5O yield two-body H loss.[8,9,40] As such, we would like to understand if/in what quantity H + C_3H_6O is formed in *i*-C_3H_7O dissociation. In coincident detection, it is challenging to detect both fragments in an H loss event because of their large mass ratio; in general, the light fragment scatters beyond the detector and the heavy fragment does not clear the beam block. Furthermore, the H atom has low translational energy in the laboratory frame so its detection efficiency is low (on the order of 0.08).[8,41] However, with sufficient translational energy release, the heavy fragment clear the beam block and hit the detector. As such, we can examine the all-fragment time-of-flight data to understand the contributions from each of our coincidence channels, and other fragments detected not in coincidence (i.e. the heavy fragment from an H loss channel). We carried out this procedure for the *i*-C_3D_7O results where the smaller fragment mass ratio for D atom loss allows for greater chance of detecting the heavy fragment.

Figure 7 compares the experimental time-of-flight distribution (black dots) to a simulation (red dots). The simulation assumes a beam energy of 6 keV, and the arrival times are referenced to the detector gate timing (the x-axis scale of 200-800 ns does not present the actual flight time but rather the arrival time for the window of detection).

The experimentally determined translational energy and angular distributions for the deuterated results of channels 1, 5, 9 and 10 were used to simulate the time-of-flight distributions for each channel. This component is shown in blue in Fig. 7. The orange trace in Fig. 7 presents the simulated contribution from D + C_3D_6O. No two-body coincident events for this channel are detected, but the heavy fragment, should it clear the beam block, arrives in a relatively narrow time interval as shown in the orange trace. D atoms with low translational energy release may also be detected but are spread out in time. The orange trace was simulated using an input translational energy distribution peaking around 3.0 eV (inset of Fig. 7) with an isotropic angular distribution. Even for events with a high translational energy release (>3 eV), the orange trace is restricted by conservation of energy, and the remainder of the fit is captured by noise, which would be expected in the all fragment time-of-flight distribution.

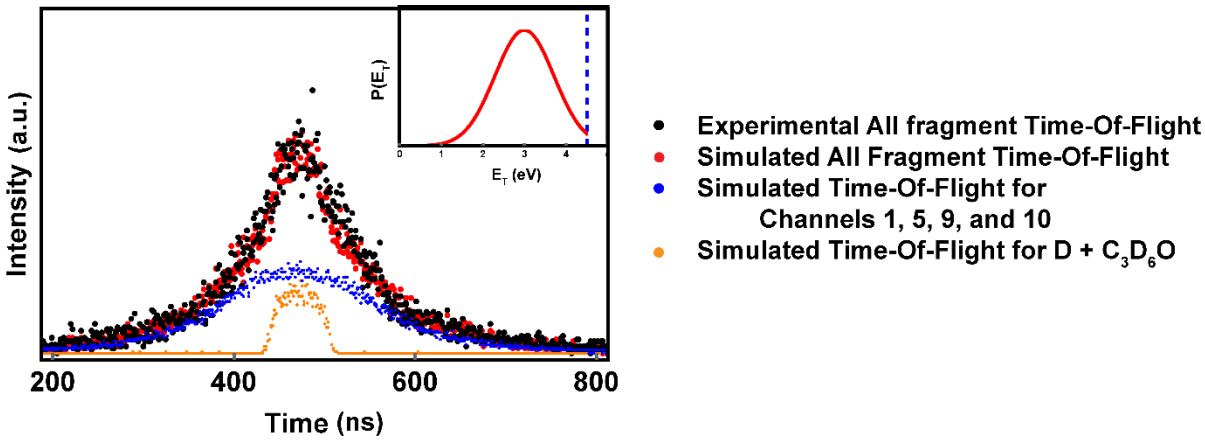

Figure 7: Experimental (black) and simulated (red) all fragment time-of-flight distributions of *i*-C_3D_7O to determine contribution of D atom loss. The blue trace is the simulated time-of-flight distribution for channels 1 (CD_3 + CD_3CDO), 5 (OD + C_3D_6), 9 (CD_3 + CD_4 + CO) and 10 (CD_3 + CD_3 + DCO) and includes two- and three-body coincident events in addition to contributions from true events in which only one or two fragments hit the detector, out of two and three, respectively. The orange plot is that of the contribution from the D + C_3D_6O, for which coincident detection is not probable. Any D atoms that hit the detector are spread out in time, but the heavy fragment has a narrow distribution of arrival times, as shown in the orange trace. Some noise has been factored in as well. The inset presents the translational energy distribution used to simulate the D + C_3D_6O contribution (channel 2 or 4) with the maximum available energy for this channel marked by the dashed blue line.

e. Branching ratios

Table 1 presents the experimental branching ratios from the coincidence data for *i*-C_3H_7O dissociation. Branching ratios are acquired from the raw experimental counts in each channel and corrected using a one-particle detection probability of $p_{\text{one-particle}} = 0.6$.[42] By extension, two- and three-body events are corrected using $p_{\text{two-body}} = 0.36$ and $p_{\text{three-body}} = 0.22$. The errors associated with each branching ratio are the standard deviation of the ratios across a collection of data sets meaning that they are random, not systematic errors. The production of channel 5 is about half that of channel 1/3 and thereby contributes to the total photofragment yield in a significantly larger quantity than is predicted by the RRKM results in Table 2.

Table 1: Experimental Branching Ratios for *i*-C_3H_7O		
Channel	**Percentage of Coincident Total Events**	**Percentage of Total Events from Noncoincidence Simulations (from deuterated results)**
i-C_3H_7O → $CH_3 + C_2H_4O$ **(1 or 3)**	54 ± 3 %	45 %
i-C_3H_7O → $OH + C_3H_6$ **(5)**	34 ± 3 %	29 %
i-C_3H_7O → $H + C_3H_6O$ **(2 or 4)**	N/A	16 %
i-C_3H_7O → $CH_3 + CH_4 + CO$ **(9)**	8.0 ± 0.7 %	7 %
i-C_3H_7O → $CH_3 + CH_3 + HCO$ **(10)**	4.0 ± 0.4 %	3 %

The three-body branching ratios indicate that channel 9 forms twice as frequently as channel 10. Due to the ambiguity in masses, it is useful to also examine the branching ratio for the dissociation of *i*-C_3D_7O. In doing so, we find that channel 9 still dominates over channel 10 slightly with a ratio of 1.3 ± 0.3 : 1.

The right most column presents the branching ratio results from the noncoincidence simulations that include the D + C_3D_6O channel. The other channel contributions have been adjusted for the ratios observed through coincident detection (i.e. those ratios in the middle column). Perhaps the most important takeaway from these ratios is that the D/H atom loss accounts for less than either of the other two-body channels but is nevertheless significant.

f. RRKM calculations

Understanding the dynamics of dissociation can be substantially aided through Rice-Ramsperger-Kassel-Marcus calculations[43] in which the microcanonical rate constant $k(E)$ is given by

$$k(E) = \frac{W^{\ddagger}(E-E_0)}{h\rho(E)} \qquad (14)$$

where *h* is Planck's constant, $\rho(E)$ is the density of states of the reactant, and $W^{\ddagger}(E-E_0)$ is the sum of states of the transition state structure. Geometries and vibrational frequencies of structures in Figure 1 were calculated using the B3LYP/aug cc-pVDZ level of theory[44] and energies of stationary points and transition states were taken from Reference 5. The Beyer-Swinehart algorithm was used to determine the density and sum of states used in the calculations.[45] Table 2 presents the rate constants for the dissociation of *i*-C_3H_7O into two-body products.

Table 2: RRKM Rate Constants for the Dissociation of *i*-C_3H_7O	
Channel	**Rate (s^{-1})**
i-C_3H_7O → CH_3 + CH_3CHO (acetaldehyde) **(1)**	3.9×10^{13}
i-C_3H_7O → CH_3 + C_2H_3OH (vinyl alcohol) **(3)**	2.2×10^{10}
i-C_3H_7O → H + $(CH_3)_2CO$ (acetone) **(2)**	6.6×10^{12}
i-C_3H_7O → H + C_3H_5OH (2-propenol) **(4)**	6.3×10^{11}
i-C_3H_7O → $CH_3C(OH)CH_2$	1.4×10^{11}
i-C_3H_7O → OH + C_3H_6 **(5)**	1.2×10^{11}

For two-body dissociation, channel 1 is predicted to be the fastest, closely followed by H loss. However, the channel 1 rate corresponds to a timescale of 25 fs, which is much faster than the time needed for energy randomization.[46] H loss is predicted to occur an order of magnitude slower, but still at the edge of what might be expected for a statistical process. These observations suggest that RRKM cannot treat either channel accurately.

4. Discussion:

This work aims to understand not only the primary products of the dissociation of *i*-C_3H_7O, but also the mechanism through which products form. Therefore, we examine the translational energy distributions more closely. In the most straightforward of instances, ground state mechanisms are typically characterized by translational energy distributions peaking near 0 eV associated with an isotropic angular distribution. In contrast, excited state dynamics typically exhibit translational energy distributions peaking away from 0 eV (close to their $E_{T,MAX}$) with an anisotropic angular distribution.

a. Two-body dissociation

The two-body dissociation of *i*-C_3H_7O leads to CH_3 loss + C_2H_4O (channel 1 and/or 3), channel 5 (OH + C_3H_6), and channel 2 or 4 (H + C_3H_6O). We cannot distinguish between channels 1 (CH_3 + CH_3CHO) and 3 (CH_3 + C_2H_3OH) by mass, but of the two relatively low energy channels, CH_3 + CH_3CHO (channel 1) is ~ 0.4 eV lower in energy. Additionally, channel 3 requires that *i*-C_3H_7O must first isomerize to $CH_3CH(OH)CH_2\cdot$, in which the lone electron is on a terminal carbon, prior to dissociating. Thus, channel 1 is a more likely candidate. Moreover, the dissociation of acetaldehyde has been thoroughly explored and the observed three-body channels bolster our argument that the C_2H_4O is indeed acetaldehyde. As such, we move forward

employing this assumption.

The translational energy distribution of channel 1 in Fig. 4a presents a broad distribution peaking substantially away from 0 (~1-1.5 eV) that is associated with a somewhat anisotropic angular distribution. This suggests that channel 1 does not form through statistical dissociation on the ground electronic state. Although excited state dissociation is possible, the translational energy distribution peaks substantially below $E_{T,MAX}$, in contrast to the photodissociation of CH_3O to $CH_3 + O$.[8,38]. Additionally, any CH_3CHO formed with < 1.05 eV of translational energy will have sufficient internal energy to dissociate further, ultimately yielding a three-body event. As much of the intensity in Fig. 4a is above 1.05 eV, it is clear that there is substantial true two-body product yield.

Channel 2 or 4 ($H + C_3H_6O$) is identified as a product channel through the noncoincidence time-of-flight simulations discussed in Section 3.d. The input translational energy distribution for this channel peaks around 3 eV, substantially away from zero, but still ~ 1-1.5 eV below $E_{T,MAX}$ for channel 2. Note that we are blind to the heavy fragment for lower translational energy release events (those with translational energy less than ~ 0.9 eV). As such, the simulations in Section 3.d are mostly useful through their confirmation that $H + C_3H_6O$ is a valid product channel.

In Fig. 4b, the translational energy distribution for dissociation of *i*-C_3H_7O to channel 5 ($OH + C_3H_6$) is much more characteristic of a statistical ground state dissociation mechanism, in which there is little translational energy imparted to the fragments and the associated angular distribution is fairly isotropic. However, in examining the RRKM calculations in Table 2, we see that channel 5 is predicted to form more slowly than channels 1 and the H loss channels (2 or 4) because of the high barrier to isomerization (TS3 in Fig. 1) that must occur prior to dissociation. Thus, it is not clear that we would even observe channel 5 were it forming on the ground electronic state, but it contributes significantly to the observed photofragment yield and the translational energy and angular distributions are most consistent with ground state dynamics.

These combined observations suggest that statistical dissociation on the ground electronic state is not occurring to yield the two-body product channels, but rather that nonstatistical behavior on

the ground electronic state is most consistent with the experimental results. Channels 1 and 2 are not adequately treated by RRKM because the rates are predicted to be too fast (i.e. they are faster than the timescale for energy randomization). The translational energy distribution for channel 1 peaks far below $E_{T,MAX}$ and the angular distribution is only slightly anisotropic. As such, internal conversion to the ground electronic state followed by nonstatistical dissociation[47] is likely the best explanation for channels 1 and 2. Channel 5 formation is associated with translational energy and angular distributions that are characteristic of statistical ground state dissociation but its formation is not favored by the RRKM calculations. One possible explanation is that isomerization occurs on an excited electronic state rapidly enough to compete with internal conversion to the *i*-C_3H_7O structure that dissociates to channels 1 and 2. After this, the $CH_3CH(OH)CH_2$ can dissociate to channel 5 either on an excited state or subsequent to internal conversion to its ground state; the translational energy and angular distribution for this channel support the latter process.

We can compare our results to the photodissociation of C_2H_5O in a similar energy regime. Experiments performed in this laboratory over a decade ago dissociated C_2H_5O using 5.17 eV.[8] The translational energy distribution of $C_2H_5O \rightarrow CH_3 + CH_2O$ was broad, peaking around 1.5 eV and tailing off until ~3.0 eV with an anisotropy parameter $\beta_{lin} = 0.33$. These results are similar to those observed here for channel 1 formation. The authors used RRKM calculations and an anisotropic angular distribution to suggest that dissociation to $OH + C_2H_5$ also does not occur on the ground electronic state following statistical decomposition. Noncoincidence time-of-flight simulations were used to determine that $H + C_2H_4O$ accounted for 36% of the total photofragment yield, more than is observed in *i*-C_3H_7O. Overall, the conclusion of the C_2H_5O work was unsettled regarding the dissociation mechanisms yielding the products but the authors suggest that that at energies 4-5 eV above the respective dissociation barriers, dissociation is just too fast on the ground electronic state to come from full statistical redistribution of the internal energy. This argument is similar to that what is observed in this work, specifically that the RRKM rates are too fast for CH_3 and H loss to come from statistical decay and that OH loss contributes more than RRKM rates suggest it should. Therefore, nonstatistical dissociation on the ground state is most consistent with the observed results.

b. Three-body dissociation

We are also interested in categorizing the formation of channels 9 ($CH_3 + CH_4 + CO$) and 10 ($CH_3 + CH_3 + HCO$), which most likely arise from secondary dissociation of acetaldehyde (CH_3CHO) formed in channel 1. These account for about 12% of the coincident dissociation events observed. As discussed in the preceding section, any CH_3CHO formed in a two-body dissociation event with less than 1.05 eV of translation energy can in principle have enough energy to dissociate further to either $CH_3 + HCO$ (channel 10) or $CH_4 + CO$ (channel 9) assuming no internal excitation of the CH_3 co-fragment. The Dalitz plots in Figs. 6a and 6b are indicative of a mechanism in which a CH_3 fragment contains a relatively consistent fraction of the translational energy release, which would be true if CH_3 leaves first. The remaining three-body products then stem from CH_3CHO secondary dissociation.

The unimolecular decomposition of CH_3CHO has been the subject of numerous experimental[48-58] and theoretical studies[59-68] because it is a small, model system that, in some instances, involves a "roaming" transition state to yield $CH_4 + CO$ products. Figure 8 depicts a basic potential energy surface for decay channels from CH_3CHO with energies referenced to *i*-C_3H_7O. In general, it has been found that $CH_4 + CO$ can form through a tight 3-center transition state[61] (over a ~ 3.9 eV barrier) or through a roaming mechanism in which ground state CH_3CHO decays to $CH_3 + HCO$ but the CH_3 abstracts H as it departs, ultimately producing $CH_4 + CO$.[49,59] In addition to $CH_4 + CO$ products, CH_3CHO can dissociate into $CH_3 + HCO$.[49,50,55]

The dynamics regarding *i*-C_3H_7O dissociation to channel 9 ($CH_3 + CH_4 + CO$) and channel 10 ($CH_3 + CH_3 + HCO$) are further ambiguous because we are investigating the secondary dissociation of CH_3CHO. As such, we have limited information about the internal energy of CH_3CHO and its effect on competing decay mechanisms, especially because we have concluded that channel 1 is formed in a nonstatistical manner. Much of the work examining CH_3CHO photolysis involves excitation to the S_1 state that can undergo intersystem crossing to the T_1 state or internal conversion back to the ground electronic state.[56,58,69] We assume in this work that we are making channel 1 products in their ground electronic states. It has been shown[56,58,69] in numerous instances that dissociation of CH_3CHO on its S_0 potential energy surface can yield both $CH_4 + CO$ (channel 9) and $CH_3 + HCO$ (channel 10). The translational energy distributions

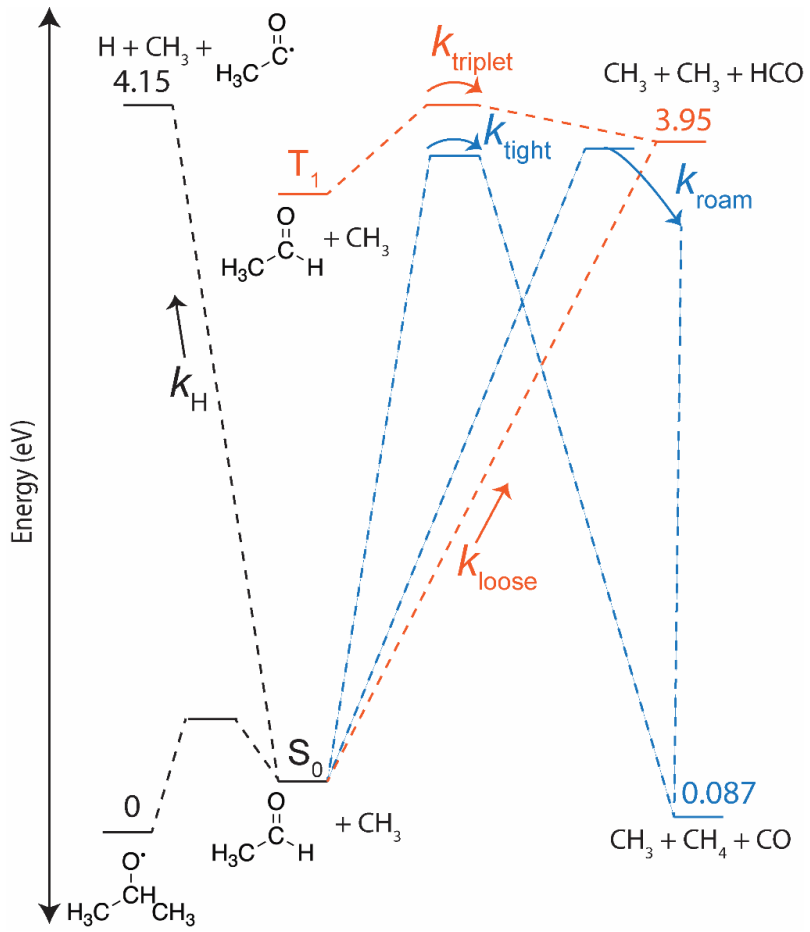

Figure 8: Potential energy surface for relevant decay channels of acetaldehyde. The orange pathways represent those that lead to channel 9 ($CH_3 + CH_4 + CO$), and the blue pathways represent those to channel 10 ($CH_3 + CH_3 + HCO$). The rate constants marked refer to that specific pathway and correspond to the associated value in Table 1. Energies for those pathways were acquired from References 59 and 60.

for each channel in this work look markedly similar, perhaps in part due to misassignment the channels. The high energy tail in Figure 5a is the only true indicator of a difference in behavior of the two channels. Additionally, our experimental branching ratios (including those for the dissociation of the deuterated isotopologue) suggest that we do observe both channels. Given that the CH_3CHO produced from channel 1 should have a range of internal energy depending upon the translational energy release of channel 1 *and* the internal energy of the CH_3 co-fragment, it is reasonable to expect that we observe both decay channels from CH_3CHO and that they are produced on the S_0 state of CH_3CHO. As has been shown,[58,59,69] the observation of roaming to

yield CH_4 + CO is highly dependent upon the available energy to CH_3CHO as it proceeds through the loose transition state to CH_3 + HCO. Therefore, as CH_3CHO could have variable internal energy after its initial formation, we cannot be confident as to whether or not a roaming mechanism is observed here.

5. Conclusions:

The photodissociation dynamics of *i*-C_3H_7O have been investigated using photofragment translational spectroscopy at 248 nm. The photofragment yield is dominated by two-body dissociation to CH_3 + CH_3CHO and OH + C_3H_6 with some contribution from H + C_3H_6O. The experimental translational energy distributions and RRKM calculations indicate that dissociation occurs primarily on the ground electronic state in a nonstatistical manner. A small amount of three-body dissociation also contributed to the total photofragment yield. Following the production of CH_3 + CH_3CHO, any CH_3CHO with sufficient internal energy can dissociate on its ground electronic state to ultimately yield CH_3 + CH_3 + HCO or CH_3 + CH_4 + CO. Dalitz plots indicate that this occurs in an asynchronous concerted manner in which only a small amount of time passes between the formation of CH_3 + CH_3CHO and the secondary dissociation of CH_3CHO to products.

The similarity of the behavior of *i*-C_3H_7O and C_2H_5O radical photodissociation leave several questions unanswered regarding the exact nature of the dynamics that yield ground state products. Future explorations into these small alkoxy systems should focus on identifying how these mechanisms occur. Nevertheless, it's clear that even the simplest of these radicals exhibit complex behavior that is pertinent to their overarching behavior in more involved chemical reactions in the atmosphere and combustion.

Conflicts of Interest:

There are no conflicts of interest to declare.

Acknowledgements:

This research was supported by the Director, Office of Basic Energy Science, Chemical Sciences Division of the U.S. Department of Energy under Contract No. DE-AC02-05CH11231. Computational work was performed through the Molecular Graphics and Computation Facility at UC Berkeley which is supported by the National Institutes of Health under Grant No. S10OD023532.

References:

1. J. J. Orlando, G. S. Tyndall and T. J. Wallington, *Chem. Rev.*, 2003, **103,** 4657-4690.
2. R. Atkinson, *Int. J. Chem. Kin.*, 1997, **29**, 99-111.
3. H. Somnitz and R. Zellner, *Z. Phys. Chem.*, 2009, **220**, 1029-1048.
4. J. Zádor, C. A. Taatjes and R. X. Fernandes, *Prog. Energy Combust. Sci.*, 2011, **37**, 371-421.
5. J. Zádor, A. W. Jasper and J. A. Miller, *Phys. Chem. Chem. Phys.*, 2009, **11**, 11040-11053.
6. T. M. Ramond, G. E. Davico, R. L. Schwartz and W. C. Lineberger, *J. Chem. Phys.*, 2000, **112**, 1158.
7. S. Gopalakrishnan, L. Zu, and T. A. Miller, *Chem. Phys. Lett.*, 2003, **380**, 749-757.
8. D. L. Osborn, D. J. Leahy and D. M. Neumark, *J. Chem. Phys.*, 1997, **101**, 6583.
9. A. E. Faulhaber, D. E. Szpunar, K. E. Kautzman and D. M. Neumark, *J. Phys. Chem. A*, 2005, **109**, 10239-10248.
10. S. C. Foster, Y.-C. Hsu, C. P. Damo, X. Liu, C.-Y. Kung and T. A. Miller, *J. Chem. Phys.*, 1986, **90**, 6766-6769.
11. C. C. Carter, J. R. Atwell, S. Gopalakrishnan and T. A. Miller, *J. Phys. Chem. A*, 2000, **104**, 9165-0170.
12. J. Liu, D. Melnik and T. A. Miller, *J. Chem. Phys.*, 2013, **139**, 094308.
13. R. Chhantyal-Pun, M. Roudjane, D. G. Melnik, T. A. Miller and J. Liu, *J. Phys. Chem. A*, 2014, **118**, 11852-11870.
14. G. B. Ellison, P. C. Engelking and W. C. Lineberger, *J. Phys. Chem.*, 1982, **86**, 4873-4878.
15. J. J. Dillon and D. R. Yarkony, *J. Chem. Phys.*, 2009, **130**, 154312.
16. L. K. Huynh, H. R. Zhang, S. Zhang, E. Eddings, A. Sarofim, M. E. Law, P. R. Westmoreland and T. N. Truong, *J. Phys. Chem. A.*, 2009, **113**, 3177-3185.
17. C.-W. Zhou, Z.-R. Li and X.-Y. Li, *J. Phys. Chem. A*, 2009, **113**, 2372-2382.
18. J.-C. Loison, J. Daranlot, A. Bergeat, F. Caralp, R. Mereau and K. M. Hickson, *J. Phys. Chem. A*, 2010, **114**, 13326-13336 .
19. J. Badra, F. Khaled, B. R. Giri and A. Farooq, *Phys. Chem. Chem. Phys.*, 2015, **17**, 2421-2431.
20. M. Szori, Christa, Fittschen, I. G. Csizmadia and B. Viskolcz, *J. Chem. Theory Comput.*, 2006, **2**, 1575-1586.

21. B. Ruscic and D. H. Bross, Active Thermochemical Tables (ATcT) values based on ver.1.122d of the Thermochemical Network, 2018, available at ATcT.anl.gov.
22. D. R. Cyr, D. J. Leahy, D. L. Osborn, R. E. Continetti and D. M. Neumark, *J. Chem. Phys.*, 1993, **99**, 8751-8764.
23. D. L. Osborn, H. Choi, D. H. Mordaunt, R. T. Bise, D. M. Neumark and C. M. Rohlfing, *J. Chem. Phys.*, 1997, **106**, 3049-3066.
24. A. W. Harrison, M. Ryazanov, E. N. Sullivan and D. M. Neumark, *J. Chem. Phys.*, 2016, **145**, 024305.
25. D. Irimia, R. Kortekaas and M. H. M. Janssen, *Phys. Chem. Chem. Phys.*, 2009, **11**, 3958-3966.
26. D. Irimia, D. Dobrikov, R. Kortekaas, H. Voet, D. A. van den Ende, W. A. Groen and M. H. Janssen, *Rev. of Sci. Instrum.*, 2009, **80**, 113303.
27. J. M. B. Bakker, *J. Phys. E: Sci. Instrum.*, 1973, **6**, 785-789.
28. J. M. B. Bakker, *J. Phys. E: Sci. Instrum.*, 1974, **7**, 364-368.
29. V. Dribinski, A. Ossadtchi, V. A. Mandelshtam and H. Reisler, *Rev. Sci. Instrum.*, 2002, **73**, 2634-2642 .
30. O. Jagutzki, A. Cerezo, A. Czasch, R. Dörner, M. Hattas, M. Huang, V. Mergel, U. Spillman, K. Ullmann-Pfleger, T. Weber, H. Schmidt-Böcking and G. D. W. Smith, *IEEE Trans. Nucl. Sci.*, 2002, **49**, 2477-2483.
31. A. W. Harrison, J. S. Lim, M. Ryazanov, G. Wang, S. Gao and D. M. Neumark, *J. Phys. Chem. A*, 2013, **117**, 11970-11978.
32. R. N. Zare, *Mol. Photochem.*, 1972, **4**, 1-37.
33. M. H. Matus, M. T. Nguyen, and D. A. Dixon, *J. Phys. Chem. A.*, 2007, **111**, 113-126.
34. B. Nichols, E. N. Sullivan, M. Ryazanov, C. M. Hong and D. M. Neumark, *J. Chem. Phys.*, 2017, **147**, 134304.
35. E. N. Sullivan, B. Nichols and D. M. Neumark, *J. Chem. Phys.*, 2018, **148**, 044309.
36. R. H. Dalitz, *Philos. Mag.*, 1953, **44**, 1068-1080.
37. C. Maul and K.-H. Gericke, *Inter. Rev. Phys. Chem.*, 1997, **16**, 1-79.
38. P. E. Crider, A. W. Harrison, and D. M. Neumark, *J. Chem. Phys.* 2011, **134**, 134306.
39. N. Neumann, D. Hant, L. P. Schmidt, J. Titze, T. Jahnke, A. Czasch, M. S. Schoffler, K. Kreidi, O. Jagutzki, H. Schmidt-Böcking, and R. Dörner, *Phys. Rev. Lett.* 2010, **104**, 103201.
40. D. L. Osborn, D. J. Leahy, E. M. Ross, and D. M. Neumark, *Chem. Phys. Lett.* 1995, **235**, 484.
41. D. E. Szpunar, A. E. Faulhaber, K. E. Kautzman, P. E. Crider II, and D. M. Neumark, *J. Chem. Phys.*, 2007, **126**, 114311.
42. M. Ryazanov, A. W. Harrison, G. Wang, P. E. Crider and D. M. Neumark, *J. Chem. Phys.*, 2014, **140**, 234304.
43. R. A. Marcus and O. Rice, *J. Phys. Chem.*, 1951, **55**, 894-908.
44. Gaussian 09, Revision D.01, M. J. Frisch, G. W. Trucks, H. B. Schlegel, G. E. Scuseria, M. A. Robb, J. R. Cheeseman, G. Scalmani, V. Barone, B. Mennucci, G. A. Petersson, H. Nakatsuji, M. Caricato, X. Li, H. P. Hratchian, A. F. Izmaylov, J. Bloino, G. Zheng, J. L. Sonnenberg, M. Hada, M. Ehara, K. Toyota, R. Fukuda, J. Hasegawa, M. Ishida, T. Nakajima, Y. Honda, O. Kitao, H. Nakai, T. Vreven, J. J. A. Montgomery, J. E. Peralta, F. Ogliaro, M. Bearpark, J. J. Heyd, E. Brothers, K. N. Kudin, V. N. Staroverov, T. Keith, R. Kobayashi, J. Normand, K. Raghavachari, A. Rendell, J. C. Burant, S. S.

Iyengar, J. Tomasi, M. Cossi, N. Rega, J. M. Millam, M. Klene, J. E. Knox, J. B. Cross, V. Bakken, C. Adamo, J. Jaramillo, R. Gomperts, R. E. Stratmann, O. Yazyev, A. J. Austin, R. Cammi, C. Pomelli, J. W. Ochterski, R. L. Martin, K. Morokuma, V. G. Zakrzewski, G. A. Voth, P. Salvador, J. J. Dannenberg, S. Dapprich, A. D. Daniels, O. Farkas, J. B. Foresman, J. V. Ortiz, J. Cioslowski and D. J. Fox, Gaussian, Inc., Wallingford, CT, USA, 2013.
45. T. Beyer and D. F. Swinehart, *Commun. ACM*, 1973, **16**, 379.
46. R. D. Levine, *Molecular Reaction Dynamics*. (Cambridge University Press, New York, New York, 2005).
47. B. Jayee and W. L. Hase, *Ann. Rev. Phys. Chem.*, 2020, **71**, 289-313.
48. A. Horowitz and J. G. Calvert, *J. Phys. Chem.*, 1982, **86**, 3105-3114.
49. M. Baba, I. Hanazaki and U. Nagashima, *J. Chem. Phys.*, 1985, **82**, 3938-3947.
50. S.-H. Lee and I.-C. Chen, *J. Chem. Phys.*, 1996, **105**, 4597.
51. H. A. Cruse and T. P. Softley, *J. Chem. Phys.* 2005, **122**, 124303.
52. P. L. Houston and S. H. Kable, *PNAS*, 2006, **103**, 16079-16082.
53. L. Rubio-Lago, G. A. Amaral, A. Arregui, J. G. Izquierdo, F. Wang, D. Zaouris, T. N. Kitsopoulos and L. Bañares, *Phys. Chem. Chem. Phys.*, 2007, **9**, 6123-6127.
54. B. R. Heazlewood, M. J. T. Jordan, S. H. Kable, T. M. Selby, D. L. Osborn, B. C. Shepler, B. J. Braams and J. M. Bowman, *PNAS*, 2008, **105**, 2719-12724.
55. S.-H. Lee, *J. Chem. Phys.*, 174312, **131**, 174312.
56. B. R. Heazlewood, S. J. Rowling, A. T. Maccarone, M. J. T. Jordan and S. H. Kable, *J. Chem. Phys.*, 2009, **130**, 054310.
57. S. Wang, D. F. Davidson, and R. K. Hanson, *J. Phys. Chem. A*, 2016, **120**, 6895-6901.
58. C.-H. Yang, S. Bhattacharyya, L. Liu, W.-H. Fang, and K. Liu, *Chem. Sci.* (2020)
59. L. B. Harding, Y. Georgievskii and S. J. Klippenstein, *J. Phys. Chem. A*, 2010, **114**, 765-777.
60. K. C. Thompson, D. L. Crittenden, S. H. Kable and M. J. T. Jordan, *J. Chem. Phys.*, 2006, **124**, 044302.
61. J. S. Yadav and J. D. Goddard, *J. Chem. Phys.*, 1986, **84**, 2682-2690.
62. B. J. Smith, M. T. Nguyen, W. J. Bouma and L. Radom, *J. Am. Chem. Soc.*, 1991, **113**, 6452-6458.
63. H. Tachikawa and N. Ohta, *Chem. Phys. Lett.*, 1994, **224** 465-469.
64. B. C. Shepler, B. J. Braams and J. M. Bowman, *J. Phys. Chem. A*, 2007, **111**, 8282-8285.
65. Y.-C. Han, B. Shepler and J. M. Bowman, *J. Phys. Chem. Lett.*, 2011, **2**, 1715-1519.
66. B. Fu, Y.-C. Han, J. M. Bowman, L. Angelucci, N. Balucani, F. Leonori, P. Casavecchia, *PNAS*, 2012, **109**, 9733-9738.
67. B. Fu, Y.-C. Han, J.M. Bowman, *Faraday Discuss.*, 2012, **157**, 27-39.
68. Y.-C. Han, P.-Y. Tsai, J. M. Bowman and K.-C. Lin, *Phys. Chem. Chem. Phys.*, 2017, **19**, 18628.
69. L. Rubio-Lago, G. A. Amaral, A. Arregui, J. González-Vázquez and L. Bañares, *Phys. Chem. Chem. Phys.*, 2012, **14**, 6067-6078.